

# We are IntechOpen, the world's leading publisher of Open Access books Built by scientists, for scientists

**6,900**

Open access books available

**186,000**

International authors and editors

**200M**

Downloads

**154**

Countries delivered to

**TOP 1%**

most cited scientists

**12.2%**

Contributors from top 500 universities



**WEB OF SCIENCE™**

Selection of our books indexed in the Book Citation Index  
in Web of Science™ Core Collection (BKCI)

Interested in publishing with us?  
Contact [book.department@intechopen.com](mailto:book.department@intechopen.com)

Numbers displayed above are based on latest data collected.

For more information visit [www.intechopen.com](http://www.intechopen.com)



# Semiconductor Nanowires: Raman Spectroscopy Studies

---

Marta De Luca and Ilaria Zardo

Additional information is available at the end of the chapter

<http://dx.doi.org/10.5772/65113>

---

## Abstract

Nanowires (NWs) are filamentary crystals with diameters of tens of nanometers and lengths of few microns. Semiconductor NWs have recently attracted a great interest, because they are emerging as building blocks for novel nanoscale devices. Since physical properties are size dependent, NWs display novel properties with respect to their bulk counterparts. Raman scattering is a nondestructive inelastic light scattering technique enabling the assessment of fundamental properties of NWs, such as crystal phase, electronic band structure, composition, and strain field. Here, we summarize the basic principles of Raman spectroscopy and measurement setup, with focus on the scattering geometries typically used for NWs. We show that changing experimental conditions, such as light polarization, excitation energy, and pressure, allows gaining information on specific NW properties, even in a spatially resolved manner along the NW length. As examples, we discuss Ge and GaAs NWs to highlight some differences between Raman spectra of NWs and the bulk, GaAs NWs to show how Raman permits to establish the crystal phase, and InGaAs/GaAs core/shell nanoneedles to explain how compositional homogeneity and strain field can be addressed by Raman spectroscopy. Finally, we discuss resonant Raman experiments on wurtzite InAs NWs that allowed the determination of their electronic band structure.

**Keywords:** inelastic light scattering, semiconductor nanowires, crystal phases, compositional disorder, strain, resonant Raman spectroscopy

---

## 1. Introduction: the world of nanowires

Semiconductor nanowires (NWs) are promising structures in the field of nanoscience. The name nanowire derives from the filamentary shape of these nanostructures. Indeed, they

have two dimensions in the range of few to tens of nanometers, while the third dimension is much longer, in the micrometer range. Typical NWs with a filamentary shape are shown in **Figure 1(a)**. The gold nanoparticles, which act as catalysts during the growth, are clearly visible.

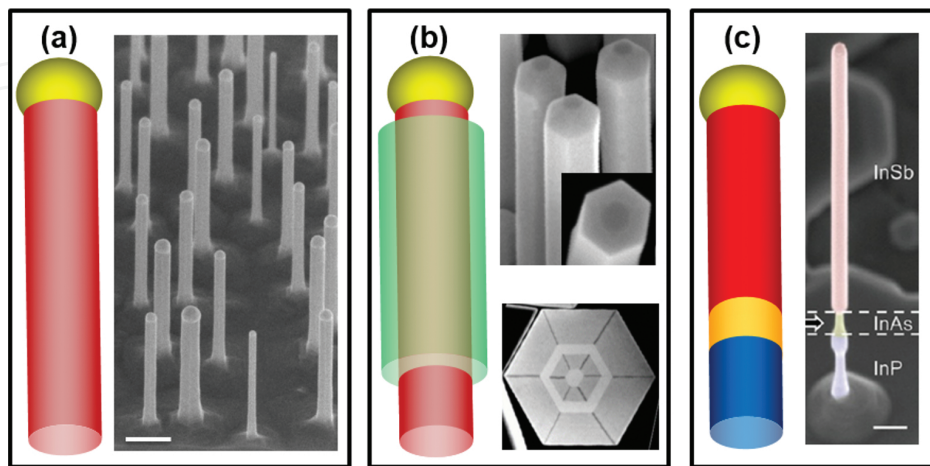


**Figure 1.** (a) Schematic and SEM image of gold-catalyzed InAs NWs. Scale bar is 200 nm. Courtesy of Dr. L. Sorba, NEST (Pisa, Italy). (b) Schematic of a radial heterostructure, with top-view SEM image of InAs-GaSb core-shell NWs (upper panel) and cross-sectional TEM image of core-multishell GaAs/AlGaAs NW heterostructures (lower panel). Courtesy of Dr. L. Sorba, NEST (Pisa, Italy) and Dr. G. Koblmuller, Walter Schottky Institut and Physik Department (Munchen, Germany), respectively. (c) Sketch of an axial NW heterostructure, together with a SEM image of an InP-InAs-InSb NW. Scale bar is 200 nm. Reproduced with permission from Ref. [3]. © 2012, American Chemical Society.

In 1991, K. Hiruma et al. accidentally grew InAs nanowires on GaAs substrates [1]. Since the time, when the word “nanowire” first appeared in a paper, NWs have attracted interest from a large number of scientists around the world owing to the extraordinary opportunities that they enable. In fact, NWs are smaller than bulk crystals and larger than nanocrystals, thus providing a natural bridge between macroscopic and microscopic worlds in both research and technology fields. Moreover, due to the anisotropic shape of NWs and their high surface-to-volume ratio, finite-size and surface/interface effects are more important than the (more known) quantum confinement effects, a circumstance that renders NWs an ideal platform for the discovery of a variety of novel phenomena.

Semiconductor NWs can exist in many different chemical compositions, structures, and shapes. Regarding the chemical composition, NWs can be made by elemental semiconductors like Si and Ge, or by III-V compounds (e.g., GaAs), II-VI compounds (e.g., CdSe), III-V alloys (e.g., InGaAs), III-nitrides (e.g., GaN), oxides (e.g., ZnO), etc. Not only homogeneously composed NWs exist, but also different materials can be mixed together in the same NW to form heterostructured NWs. Heterostructures are typically prepared in two ways [2]. In radial structures, one or more materials are grown around a NW, in a so-called core-shell or core-multishell arrangement. **Figure 1(b)** shows a schematic of this kind of structures along with a scanning electron microscope image (SEM) of an InAs-GaSb core-shell NW and a cross-section transmission electron microscopy (TEM) image of a core-multishell GaAs/AlGaAs NW. In axial structures, the NW composition is varied along the NW main axis, as depicted in **Figure 1(c)**,

whereas an SEM image of an InP/InAs/InSb axial heterostructure is also displayed [3]. In the NW form, highly mismatched materials can grow on top of each other without misfit dislocations, due to the NW capability to accommodate strain by a coherent expansion of the lattice outward.

Regarding the shape, NWs have been grown in many different, sometimes funny, shapes that could add functionalities to nanoscale devices [4]. For instance, NWs were grown in branched or flower-like morphologies [5], where an increased surface area ensures higher power-conversion efficiency compared to straight and vertical NWs.

NWs are the nanomaterial system in which pivotal key parameters, such as composition, structure, morphology, and doping, have been best controlled to date. At the heart of this control is the development of successful methods for NW growth. In the top-down technology, lithographic techniques allow to carve the nanowire structure out of a bulk material. This kind of approach ensures fine control over the position of the NWs, but the crystal quality of the NWs is not excellent (due to the surface damage produced by etching processes), and large-area production is problematic and expensive. Therefore, bottom-up NW fabrication is the most diffused. Since one-dimensional growth on a substrate is not energetically favored with respect to a two-dimensional growth, a change of the initial surface/interface is required to activate the NW growth. This change can be done by creating holes in the substrate (selective area growth) or by using metal particles, such as gold, to induce the crystal growth (particle-assisted growth) via the so-called “vapor-liquid-solid” (VLS) mechanism that was first invoked in the 1960s to explain the growth of Si whiskers [6]. In both cases, epitaxial techniques are employed to fabricate NWs. In **Figure 2**, the main steps of a typical VLS growth process leading

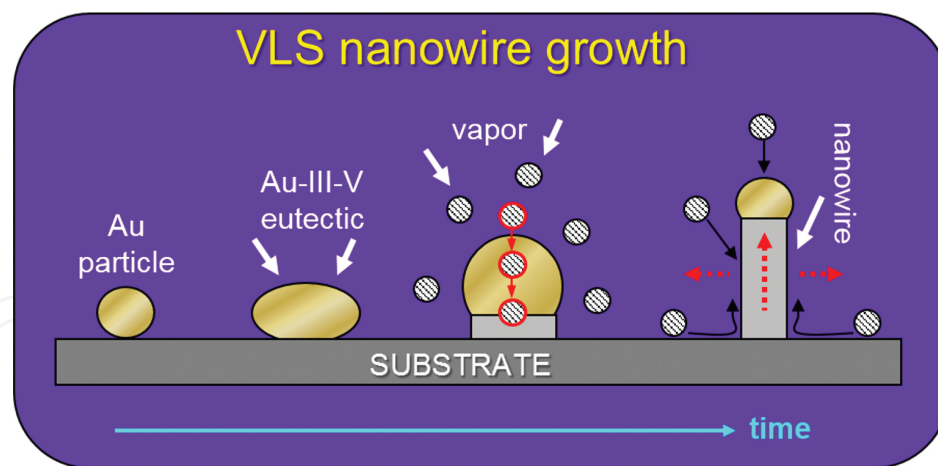


**Figure 2.** Main steps of the VLS growth process of III-V nanowire grown by metal-organic vapor phase epitaxy (MOVPE). First, a gold particle (with diameter <100 nm) is deposited/formcd on a substrate made by III-V crystal. Then, the particle is heated until it melts. The liquid droplet often consists of a molten eutectic alloy between Au and the substrate. Afterwards, group-III and group-V precursors in the vapor phase are introduced. They do not decompose on the solid substrate, as typically the temperature used during growth is too low. Decomposition only occurs at the droplet interface due to the catalytic effect of the metal. The red path represents absorption, diffusion in the liquid droplet, and precipitation of adatoms at the base of the droplet. The precipitation is due to the continued incorporation into the liquid droplet leading to a supersaturation. Finally, axial and radial growth of the NW occurs as soon as additional material precipitates on the growth interface. The three possible diffusion paths of adatoms before adsorption are sketched by black arrows.

to free-standing III–V NWs are explained, since this is the most widely used technique to grow high-quality nanowires. Each gold droplet represents the nucleation site of a NW, so there are approximately as many NWs as the droplets are. The gold droplets can be directly deposited on the substrate or result from the annealing of an Au thin film. To achieve a perfect control on the NW position, an array of gold particles can be even prepared by using lithography techniques.

Thanks to the high degree of control reached on the NW growth process, nowadays most of NW properties can be finely tuned, to such an extent that the creation of NWs tailor fit to specific applications is close to be achieved. Due to the several technological applications enabled by NWs, the interest of the scientific community on them is rapidly growing, as testified by the exponentially growing number of papers published on NWs in the last two decades. The field where the peculiar shape and dimensions of NWs have revealed to have great potential in enabling new functions and/or simply enhancing performances of existing devices is very broad, as it includes electronics, photonics, biosensing, energy conversion, and storage [7]. Therefore, we will pick few examples taken from such a huge variety. For instance, the capability to controllably dope NWs is routinely exploited in field effect transistors [8] while the low mass peculiar to NWs renders them ideal to be used in cantilever force sensors [9] and the NW flexibility makes them easily integrable in devices like flexible displays and artificial skin [10]. Moreover, the NW diameter, smaller than the light wavelength in the visible range, allows NWs to confine electromagnetic waves in the radial direction while guiding light in the axial direction, a property that has been exploited to build NW-based antennas, lasers, and light-emitting diodes (LEDs). An example of a multicolor NW-based LED is shown in **Figure 3(a)** [11]. In the field of energy conversion, we mention that the typically low thermal

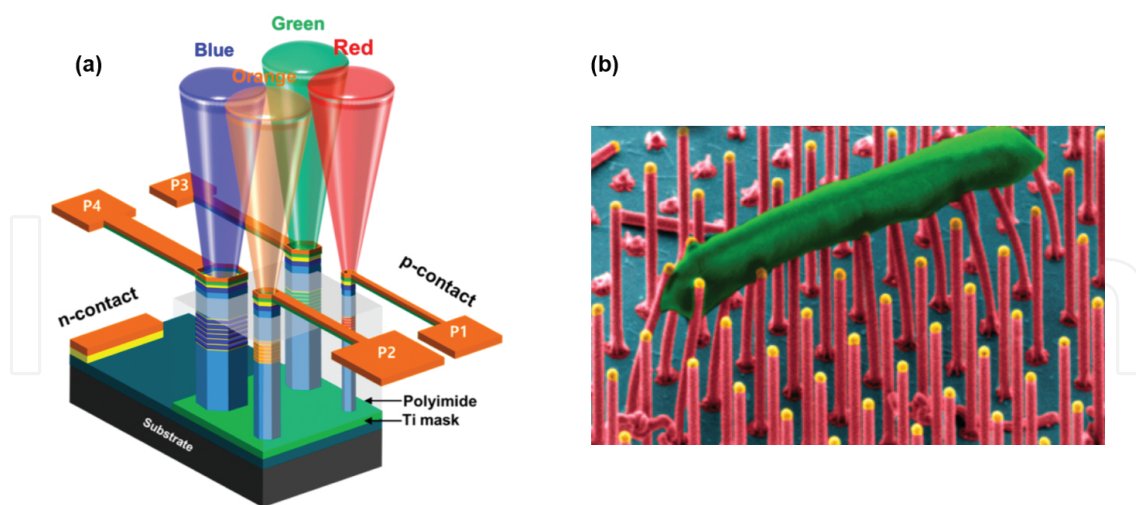


**Figure 3.** Two very recent examples of the technological power of NWs. (a) Schematic of monolithically integrated multicolor single InGaN/GaN dot-in-nanowire LED pixels on a single chip. Light emission wavelength is tuned across the visible spectrum by varying the nanowire diameter. Reproduced with permission from [11]. Copyright 2016, American Chemical Society. (b) SEM image showing the deformation of an array of InP NWs in direct contact with the body of a phytopathogen *Xylella fastidiosa* cell (colorized in green). The ordered NW array allows to evaluate single cell adhesion forces and to explore their dependence on organochemical surface compositions. Reproduced with permission from Ref. [14]. © 2016, American Chemical Society.

conductivity of NWs makes them ideal building blocks of thermoelectric devices able to convert wasted heat into electricity [12], while the high surface-to-volume ratio of NWs ensures great light absorption capability, which is currently exploited in the fabrication of high-efficiency solar cells [13]. Finally, interfacing NWs with living cells for delivering drugs or doing sensing activity is a very fascinating field. As an example, in **Figure 3(b)** we show an array of NWs acting as force sensors for bacterial cell adhesion [14].

After this brief overview on the NW world, including growth processes and technological applications, we will describe the properties of NWs that can be addressed by Raman spectroscopy. Indeed, a deep understanding of the NW properties is the starting point to design powerful devices as well as to perform important fundamental physics studies.

## 2. Experimental setup for Raman spectroscopy in nanowires

Whenever an electromagnetic radiation heats a sample, the light interacts with the sample. It may be reflected, absorbed or scattered. Raman spectroscopy relies on inelastic scattering of the radiation by the sample. It is a versatile and nondestructive technique based on the interaction between the radiation and the vibrational and/or rotational motions of the ions and it provides information such as crystal symmetry, composition, strain, lattice dynamics, and electronic band structure. In a Raman experiment, a monochromatic light is usually sent on the sample and the scattered light is collected and analyzed. When the frequency of the scattered radiation is analyzed, there will be not only the incident radiation wavelength (elastic or Rayleigh scattering component) but also radiation scattered at frequencies lower (Stokes) or higher (anti-Stokes) than the elastic one (inelastic scattering or Raman components). The intensity of the elastic component is much higher than the inelastic ones, thus special tricks are used to detect the weak Raman signal. Furthermore, the Stokes peak has intensity higher than the anti-Stokes peak, and their intensities depend on the temperature. The inelastic peaks appear at frequencies that differ from the incident one by a quantity called Raman shift, independent of the excitation frequency. The Raman shift is the most significant information in a Raman experiment.

In a typical Raman setup, the excitation energy is provided by a monochromatic laser source emitting in the visible range (488, 514, and 633 nm are the most common wavelengths). The laser light is filtered by a laser band pass filter and its polarization is cleaned from possible depolarized contributions with the use of a polarizer. Then, the beam is guided toward the sample with a set of mirrors and a polarization preserving beam splitter (typically 50:50). If nanostructures are investigated, like in our case, the laser light is focused via a microscope objective. A good objective has a high numerical aperture ( $\sim 0.9$  for  $100\times$  magnification), which results in a diffraction-limited laser spot able to provide submicrometric resolution. The nanostructure is positioned on an  $x-y$  piezoelectric stage, in such a way that its surface can be automatically scanned with high precision. The scattered Raman signal is collected by the same objective in the so-called backscattering geometry and focused to the entrance slit of a spectrometer equipped with diffraction gratings (typically with 1800 lines/mm). The signal is

dispersed in the spectrometer and then sent to a Si multichannel charge coupled device (CCD) detector. When standard, namely single stage spectrometers are used, a notch filter before the spectrometer is necessary to reject the intense elastic component, and only Raman shift larger than  $\sim 50 \text{ cm}^{-1}$  can be detected. The best spectrometers existing for Raman spectroscopy are triple-stage spectrometers, where no notch is required, because the first two gratings are used for the rejection of the elastic contribution and of the stray light (in the so-called “subtractive mode”), while the third grating disperses the radiation components and determines the resolution. To provide an idea, a 1800 lines/mm grating mounted on a spectrometer with 0.5 m focal length gives a resolution of  $\sim 0.7 \text{ cm}^{-1}$ . After the measurements, an accurate frequency calibration of the Raman spectra is usually performed exploiting the well-known energies of the emission lines of a neon lamp.

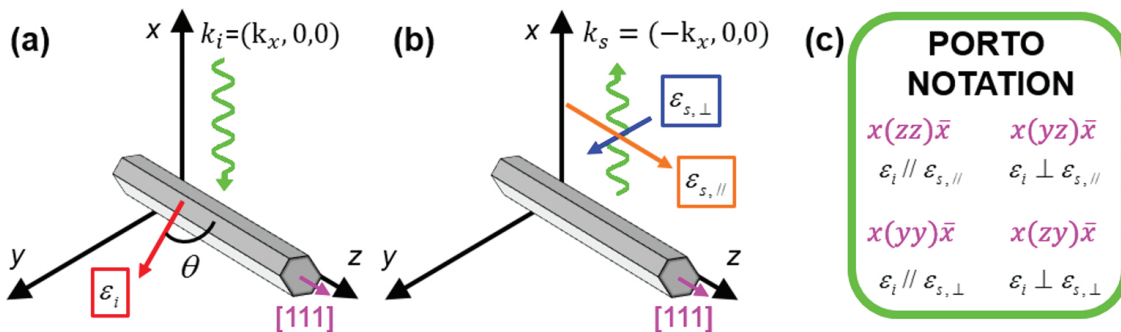


**Figure 4.** Sketch of a typical backscattering geometry used in polarization-resolved Raman experiments on a single ZB nanowire whose growth axis is in the crystallographic direction [111], aligned with the  $z$ -axis of the reference system. (a) The incident light wavevector  $k_i$  is parallel to the  $x$ -axis and its polarization vector  $\varepsilon_i$  varies, forming an angle  $\theta$  with  $z$ . (b) The scattered light wavevector  $k_s$  is along  $-x$  and the components of its polarization vector  $\varepsilon_s$  either parallel or perpendicular to  $z$  are selected. (c) Four common scattering configurations are indicated in the Porto notation:  $k_i(\varepsilon_i, \varepsilon_s)k_s$ .

In **Figure 4**, a typical geometry for performing polarization-resolved Raman measurements on a single NW is sketched. Let us consider a NW with zinc blende (ZB) phase, grown along the [111] direction and having a hexagonal cross section, with facets of the {110} family. After transferring the wire on a substrate, the flat facet of the family {110} is perpendicular to the incident light wavevector ( $k_i$ ) and the NW long symmetry axis is aligned with the  $z$ -axis of our reference system, as schematized in (a). In the used backscattering geometry,  $k_i$  is parallel to the  $x$ -axis and the scattered light wavevector ( $k_s$ ) is opposite to it, see panel (b). As a consequence, all light polarization vectors lie in the  $yz$  plane. During the measurements, the polarization of the excitation ( $\varepsilon_i$ ) is rotated by an angle  $\theta$  with respect to the nanowire growth axis. The scattered radiation is analyzed by selecting the component of the polarization either parallel to the NW growth direction ( $\varepsilon_{s,\parallel}$ ) or perpendicular to it ( $\varepsilon_{s,\perp}$ ). In the following, we will indicate the scattering configuration in the so-called Porto notation,  $k_i(\varepsilon_i, \varepsilon_s)k_s$ , where the outer terms, from left to right, refer to the directions of exciting and scattered light, respectively, and the inner bracket refers to the excitation and detection polarizations. Some examples of the most common scattering configurations as indicated in Porto notation are given in panel (c).

From the experimental point of view,  $\varepsilon_i$  of the incoming light is rotated by an angle  $\theta$  with respect to the z-axis by using a lambda half plate whose fast axis forms an angle  $\theta/2$  with the z-axis, while a polarizer before the spectrometer is used to select the scattered radiation with components of the polarization either parallel or perpendicular to the z-axis. Since the efficiency of a spectrometer depends on the polarization of the entering light, a lambda half plate at the entrance of the spectrometer is used to flip the polarization of the light into the most efficient direction.

By measuring the dependence of the scattered intensity on the incident and scattered polarization directions one can deduce the symmetry of the Raman tensors, thus the symmetry of the corresponding phonon, based on the comparison with the theoretical calculation of the intensity of the Raman signal for that specific experimental geometry. The intensity of the scattered light  $I_s$  into a solid angle  $d\Omega$  is given by [15],

$$I_s = I_i \cdot k \cdot |\varepsilon_i \cdot R \cdot \varepsilon_s|^2 d\Omega \quad (1)$$

with  $I_i$  the irradiance of the radiation incident on the sample,  $k = 2\pi a^2 \omega_s$  ( $a = 1/137$  and  $\omega_s$  frequency of the scattered light), and  $R$  the Raman scattering tensor, which is defined as  $R = \left( \frac{d\alpha}{dQ_0} \right) \cdot Q(\omega_q)$ , where  $\alpha$  is the crystal polarizability, and  $Q$  the vector displacement of an atom induced by a phonon. It is usually convenient to transform the Raman tensors in a basis made by the three main crystallographic axes of the sample and to express the polarization vectors in that basis. From Eq. (1) one can calculate the selection rules for all modes in specific scattering geometries.

Once the basic principles of Raman spectroscopy in NWs and measurement setup have been summarized, the most significant results of Raman spectroscopy applied to NWs can be described.

### 3. Size effects in the Raman spectra of semiconductor nanowires

In a 3D-crystal with  $N$  atoms per primitive unit cell, the phonon dispersion (namely, the relation between the frequency and the wavevector of lattice vibrations) is composed of  $3N$  branches (three of them are acoustic and the remaining  $3N-3$  are optical). Along high-symmetry directions the phonons are classified as transverse or longitudinal according to whether their displacements are perpendicular or parallel to the direction of the phonon wavevector  $q$ , respectively. Due to momentum and energy conservation rules, only the optical lattice modes at  $q=0$  ( $\Gamma$  point) can be studied by one-phonon spectroscopic techniques (infrared spectroscopy for odd parity modes and Raman scattering for both odd and even parity modes). In III-V ZB crystals and group IV crystals with the diamond structure, such as Si and Ge, there are six-phonon branches (because there are two atoms per primitive unit cell): two transverse and one longitudinal acoustical modes (TA and LA, respectively) and two transverse and one longitu-

dinal optical modes (TO and LO, respectively). The TO and LO near  $\Gamma$  are degenerate only in group IV crystals since the two atoms in the unit cell are identical.

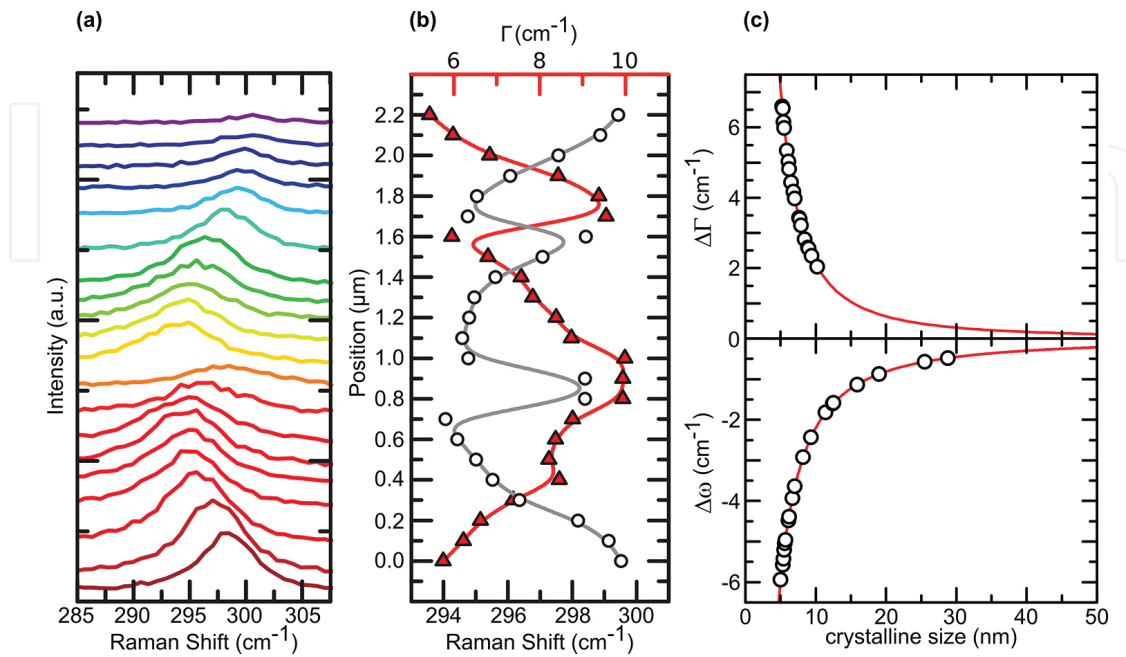


**Figure 5.** (a) Raman spectra recorded every 100 nm along a Ge NW with diameter of 86 nm. (b) Peak position (open circles, bottom scale) and FWHM  $\Gamma$  (full triangles, top scale) of the degenerate TO/LO modes as a function of the position. Solid lines are guides to the eyes. (c) Bottom: energy shift  $\Delta\omega$  from the crystalline Ge Raman peak position (298 cm<sup>-1</sup>). Top: broadening  $\Delta\Gamma$  with respect to the natural FWHM of the crystalline Ge Raman peak (3.4 cm<sup>-1</sup>). Open circles are the experimental values; solid lines come from the theoretical model.

In nanostructured materials it is usually observed that the energy of TO and LO modes is very similar to the bulk case. Differences may arise due to phonon confinement effects when scaling down the size of the crystal. Indeed, whenever the sizes of the “phonon wave packet” are comparable to the crystal size, an uncertainty in wavevector is introduced, which results in a contribution to the Raman peak at frequencies different from that at the  $\Gamma$  point. In other words, there is a relaxation of the  $q = 0$  momentum conservation rule. As a consequence, the Raman line shifts (in a direction depending on the phonon dispersion) and broadens. **Figure 5(a)** shows Raman spectra taken along a single Ge nanowire consisting of a crystalline Ge core, whose diameter is inhomogeneous along the NW length, surrounded by an amorphous Ge layer [16]. The main band, attributed to the degenerate TO/LO phonons of the core, display variations in intensity and energy along the NW axis. Panel (b) shows the peak energy (open circles) and the full width at half maximum (FWHM)  $\Gamma$  (full triangles) of the phonon band as a function of the position (with steps of 100 nm). Since the downshift is mostly accompanied by a broadening, these effects point to phonon confinement in the core. By using a proper model and taking the experimental lattice constant of Ge NWs from the literature, an estimate of the size of the nanocrystal is determined by our experimental downshift ( $\Delta\omega$ ) and broadening ( $\Delta\Gamma$ ) of the TO/LO band, as displayed in panel (c). The observed  $\Delta\omega$  correspond to a crystal size between 5 and 30 nm, in excellent agreement with the TEM analysis [16], while the

broadening gives values between 5 and 10 nm. We believe that the broadening data are less reliable because the inhomogeneity of the core in diameter (definitely probed by a  $\sim 1 \mu\text{m}$  laser spot) creates an additional broadening of the phonon band, resulting in crystal sizes smaller than the real ones.

In the context of size effects in NWs, in addition to phonon confinement also the high surface-to-volume ratio of NWs plays a role and creates differences with the bulk. As a matter of fact, the surfaces represent a new physical boundary. The crystal symmetry might be affected by the existence of the edges, which lead to a rearrangement of the lattice and can activate silent modes. Also, specific modes associated to the surface, such as surface optical (SO) modes or breathing modes, may appear [17]. The SO phonons are created at the interface between different materials with different dielectric constants and propagate along the interface. They are activated by a breaking of the translational symmetry of the surface potential, likely due to diameter variations along the NW length. Finally, since the surface atoms are “less bound” than the internal atoms, they “experience” a different local field. The propagation of optical phonons, where the oscillating dipoles, created by the out of phase oscillation of ions and cations, interact via a dipole-dipole interaction, is most affected by this.

Besides the appearance of the SO modes, the peculiar cylindrical shape with nanoscale dimensions of the NWs gives rise to the so-called dielectric mismatch effect, as will be discussed in the following. A representative example of the difference between NWs and the bulk is presented in **Figure 6** for zinc blende GaAs [18, 19]. In panel (a) we show a Raman spectrum of a ZB NW grown along the [111] direction (blue) and a spectrum of a (111)-oriented GaAs wafer (black) tilted by  $90^\circ$ . The spectra were, therefore, collected in the same scattering geometry, namely,  $x(zz)\bar{x}$ . The spectra are composed of a unique phonon mode, the  $E_1(\text{TO})$ , at  $\sim 267 \text{ cm}^{-1}$ , as expected, based on the experimental geometry and the Raman tensors for ZB. The FWHM of this mode in the NW spectrum is  $\sim 2 \text{ cm}^{-1}$  larger than in the bulk, which indicates a good crystal quality of the NW, the broadening being likely due to the presence of some twins in the crystal structure. Panel (b) displays the azimuthal dependence of parallel (full circles) and perpendicular (open squares) components of the scattered light of this mode for the bulk (left) and the NW (right). The measurements are performed as described in **Figure 4(a)** and **(b)**. In the bulk, the maximum intensity is found almost at the angles ( $\theta \sim -20^\circ$  for the parallel component and  $\theta \sim 70^\circ$  for the perpendicular) resulting from calculations based on Eq. (1). A same result is found in the NW for the parallel component. Instead, the perpendicular component is much less intense than in the bulk and it has no clear angular dependence. This difference points to a modification of the selection rules when passing from the bulk to the NW. This change can be attributed to the one-dimensional geometry of the NW. Indeed, in cylindrical-like crystals whose dielectric constant is larger than the one of the surrounding air, light absorption/emission is suppressed for light polarization perpendicular to the long symmetry axis because of image forces arising at the interface between the cylinder and its surroundings [20]. In NWs, this effect was observed also in photoluminescence measurements and it is strongly dependent on light wavelength and NW diameter. It exists in all NWs and in wurtzite NWs it has to be carefully taken into account when dealing with electronic

selection rules [21]. In Raman spectroscopy, because of this effect the phonon modes are more efficiently excited for parallel polarization, as we observe.

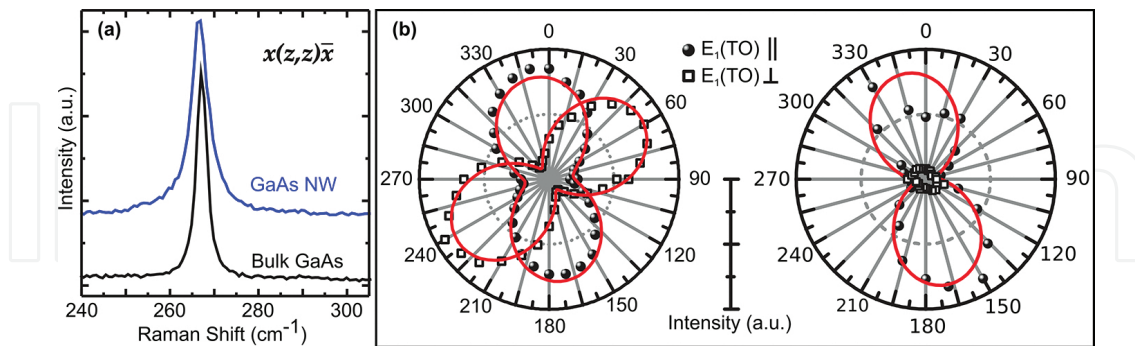


**Figure 6.** (a) Raman spectra of a NW grown along the [111] direction (blue) and of a (111)-oriented GaAs wafer (black) recorded in the same scattering geometry,  $x(z,z)\bar{x}$ . (b) Azimuthal dependence of the TO mode of the bulk GaAs (left) and of the NW (right). Full circles and open squares represent the components of the Raman signal along the  $z$ - and  $y$ -axes, respectively. Solid lines are squared sine fits to the data.

#### 4. Assessment of the crystal phase of nanowires

The crystallization of NWs in a crystalline phase that is not stable in the bulk form is one of the consequences related to the large surface-to-volume ratio of NWs, since the “unusual” crystal structure formation is favored for certain ranges of the relevant interface energies. For instance, non-nitrides III–V materials (such as GaAs, InAs, InP, etc.) that are notoriously stable in the cubic ZB phase in the bulk form can crystallize in the hexagonal wurtzite (WZ) phase when grown in the NW form under suitable VLS conditions. The occurrence of WZ in the lattice of these NWs is one of the most surprising findings in NWs and it provided the unprecedented opportunity to investigate this poorly known crystal phase. Many studies indicate that the WZ phase is favored in NWs featuring a high surface-to-volume ratio, such as in small diameters NWs [22], but an exhaustive picture of the reasons why WZ is formed in NWs is still lacking in the literature. It is worth stressing that the electronic and optical properties of the NWs strongly depend on their crystal phase [23] and thus engineering the crystal phase switching leads to the realization of heterostructures with additional degrees of freedom enabling novel optoelectronic devices [24, 25].

The differences between ZB and WZ properties are given by their different crystal structures. The ZB crystal is formed by two interpenetrating face-centered-cubic Bravais lattices (each of a different atomic species), whereas WZ is constructed from two interpenetrating hexagonal-close-packed lattices. The differences between ZB and WZ crystals are best understood by observing their structures in the [111] direction (that is the [0001] direction in WZ, usually known as the  $c$ -axis), along which both crystals look like stacked hexagonal layers, as shown in **Figure 7(a)** for a generic III–V crystal. Clearly, WZ and ZB are made by identical atoms within each layer, but these layers are alternated according to a different stacking sequence: ABABAB

in WZ and ABCABC in ZB. The length of the unit cell of the WZ phase along the [0001] direction is double of the cell of the ZB phase in the [111] direction [26]. Due to these crystallographic similarities, the principal features of the WZ electronic and phononic band structure can be understood starting from the ZB band structure and applying folding arguments. We will discuss in detail the phonon band structure, as it can be probed mainly by the Raman spectroscopy.

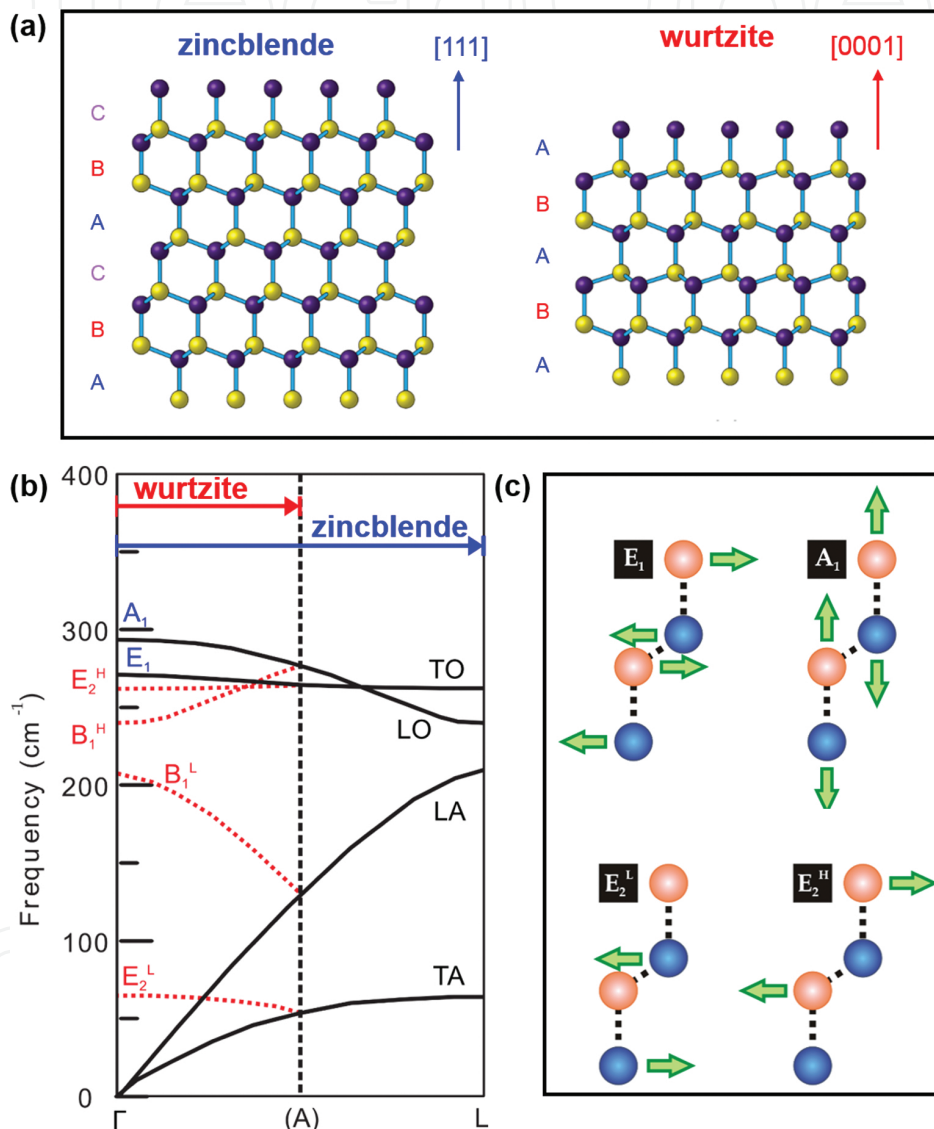


**Figure 7.** (a) Schematic drawing of the atomic arrangement in zinc blende (left) and wurtzite (right) structures of a III–V semiconductor. Each letter represents a bilayer. (b) Phonon dispersion of a typical III–V semiconductor (GaAs). The phonon branches of the ZB structure (solid lines) are folded to give rise to the phonon branches of the WZ structure (dashed lines). (c) Atomic displacements corresponding to the Raman active optical phonon modes in the WZ structure.

**Figure 7(b)** shows how the phonon dispersion of a III–V WZ crystal can be obtained by folding the one of the ZB structure along the [111] direction, namely from the  $\Gamma$  to the L point. We can

consider only this high symmetry direction because we will deal with one-phonon Raman scattering, which probes only phonons close to the  $\Gamma$  point. As discussed in the previous section for ZB GaAs crystals, there are six-phonon branches: 2TA, 1LA, 2TO, and 1LO. We stress that the dispersion curves of the TA modes are relatively flat near the zone edge and their energies are much lower than the LA phonon energy due to the covalent nature of bonds in these crystals. The LO phonon has higher energy than the TO phonons near  $\Gamma$  due to the ionic character of the bonds and the macroscopic electric field connected with the long wavelength LO phonon, at variance with group IV crystals where they are degenerate because no extra charge is carried by the two identical atoms in the unit cell.

In WZ, four new modes appear at the  $\Gamma$  point of the Brillouin zone. The folded modes are indicated with red dashed lines. Group theory predicts eight-phonon normal modes at the  $\Gamma$  point:  $2A_1 + 2E_1 + 2B_1 + 2E_2$ . Considering our scattering geometry described in **Figure 4** and the crystallographic axes of a typical WZ NW grown along the [0001] direction, only the  $A_1(\text{LO})$ ,  $E_1(\text{TO})$ ,  $E_2^H$ , and  $E_2^L$  modes can be experimentally observed. The atomic displacements associated to these modes are sketched in panel (c). The notation  $E_1$  and  $A_1$  denote modes vibrating perpendicular and along the growth axis, respectively. Since  $A_1$  and  $E_1$  modes are also found in ZB, the appearance of  $E_2^H$  and  $E_2^L$  modes in the Raman spectrum of III–V NW is the unambiguous signature of a WZ phase.

Polarization-resolved Raman measurements provide a reliable way to address the crystal phase of a given NW. To obtain such information it is necessary to calculate the selection rules for the modes specific to that crystal phase by using Eq. (1) and compare them with the experimental results. The Raman tensors of all existing crystal structures can be found in [27]. As summarized in table I in [19], in WZ III–V NWs grown along the [0001] direction (parallel to the  $z$ -axis in **Figure 4**) in backscattering configuration the  $A_1(\text{TO})$  is expected to be observed only in the  $x(yy)\bar{x}$  and  $x(zz)\bar{x}$  configurations, the  $E_2^H$  and  $E_2^L$  only in  $x(yy)\bar{x}$ , and  $E_1(\text{TO})$  in  $x(zy)\bar{x}$ . Experimentally, the selection rules can be probed by measuring the dependence of the scattered intensity on the incident and scattered polarizations as done in **Figure 6**. **Figure 8** shows how this was made in GaAs NWs [19]. In panel (a) the Raman spectra obtained under the four main polarization configurations on the same pure-phase ZB NW of **Figure 6** are displayed. Only the  $A_1/E_1(\text{TO})$  mode is visible and its intensity is maximum in the  $x(zz)\bar{x}$  configuration, as clear also in the right panel of **Figure 6 (b)**. The reason for the sizable decrease in its intensity whenever the incident or scattered light are polarized perpendicular to the NW is the dielectric constant mismatch that we discussed in Section 3. In panel (b) of **Figure 8** we show the same measurement taken on a region of pure WZ phase in a mixed WZ/ZB NW. The  $E_2^L$  is not observed due to its very low energy, the  $A_1(\text{TO})$  and  $E_1(\text{TO})$  are almost degenerate in GaAs and appear at  $\sim 266 \text{ cm}^{-1}$ . In  $x(zy)\bar{x}$  the  $A_1/E_1$  peak should be mainly  $E_1$  and in  $x(yy)\bar{x}$  and  $x(zz)\bar{x}$  mainly  $A_1$ . The shoulder at  $\sim 290 \text{ cm}^{-1}$  can be ascribed to the theoretically forbidden  $A_1(\text{LO})$ , here most probably activated by the tilted facets of the hexagonal cross-section of the NW that are not perpendicular to  $k_i$ . Most importantly, we observe the  $E_2^H$  mode at  $\sim 256 \text{ cm}^{-1}$ , with the highest intensity in the  $x(yy)\bar{x}$  configuration, as distinctive of the WZ phase. Its full azimuthal dependence in (c) for detected polarizations parallel (full circles) and perpendicular (open squares) to the NW axis nicely confirms this attribution: the maximum intensity

of both detected polarizations is found when the polarization of incident light is perpendicular to the NW axis, though for the parallel detected polarization the dependence is less clear due to the low intensity.

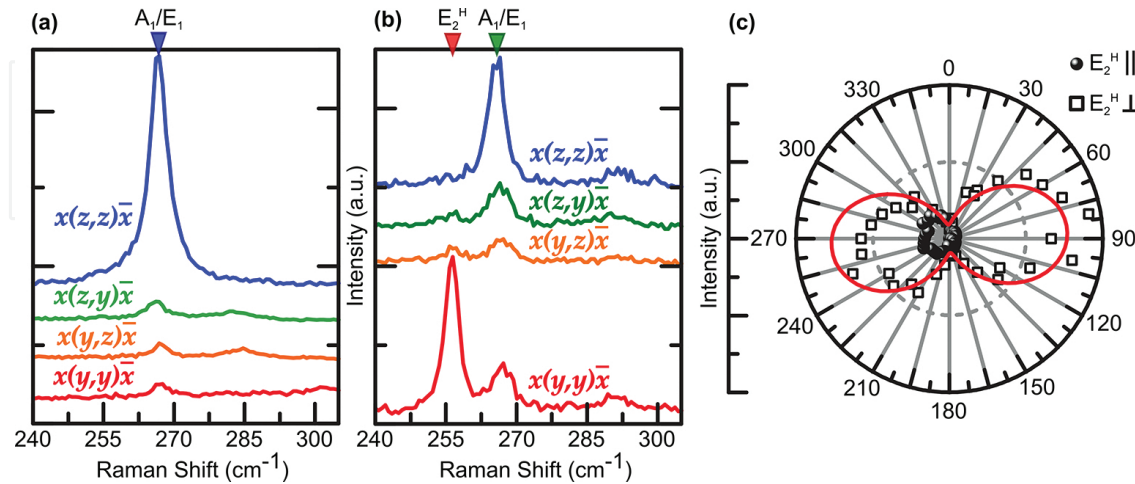


**Figure 8.** (a) Raman spectra of the ZB GaAs NW collected under the four main polarization configurations. The full azimuthal dependence is in the right panel of **Figure 6(b)**. (b) Same as (a) for a GaAs NW with WZ structure. (c) Azimuthal dependence of the parallel (full circles) and perpendicular (open squares) components of the  $E_2^H$  Raman mode with respect to NW growth axis. The solid red line is a squared sine fit to the data.

## 5. Assessment of the chemical composition and strain field in nanowires

In order to demonstrate the power of Raman spectroscopy to probe the chemical composition of NWs, it is worth focusing on alloyed NWs, while to investigate the strain state heterostructured NWs (e.g., core-shell NWs) are ideal. Here, we focus on core-shell  $\text{In}_x\text{Ga}_{1-x}\text{As}/\text{GaAs}$  NWs as they fulfill both requirements. These NWs are called nanoneedles (NNs) because they are highly tapered. They feature a highly pure WZ phase [28].

The chemical composition  $x$  of the  $\text{In}_x\text{Ga}_{1-x}\text{As}$  core can be determined by Raman spectroscopy as displayed in **Figure 9**. Raman spectra of NNs with different indium composition capped with 30 nm of GaAs are shown in panel (a). Samples are labeled with the nominal In content and spectra were taken in the  $x(yy)\bar{x}$  configuration. In agreement with the observations in **Figure 8(b)** for WZ GaAs, in  $x(yy)\bar{x}$  both  $A_1$  (TO) and  $E_2^H$  modes are observed (the  $E_2^H$  peak here is more intense than the  $A_1$ ), while in the  $x(zz)\bar{x}$  geometry (not shown here) only the  $A_1$  (TO) is observed. The shoulder at about 235  $\text{cm}^{-1}$  can be attributed either to a WZ InAs-like TO mode or to an interface mode. The Raman shift of all modes as determined by Lorentzian fits to the data (see for example the green solid lines in (a)) is reported in (c) as full squares (for data taken in  $x(yy)\bar{x}$ ) and open circles (for  $x(zz)\bar{x}$  data) as a function of the nominal In content. Solid lines represent the theoretical estimates of the GaAs-like and InAs-like modes energies obtained for ZB  $\text{In}_x\text{Ga}_{1-x}\text{As}$ . No theoretical estimate is available for WZ  $\text{In}_x\text{Ga}_{1-x}\text{As}$ , and so the energy of  $E_2^H$ , present in WZ only, has no theoretical comparison. The effective indium

compositions as extracted by the comparison between experiment and calculation for the GaAs-like TO modes are  $x = (0.22–0.24)$  for the sample with nominal  $x = 0.20$ ,  $x = (0.17–0.22)$  for nominal  $x = 0.16$ , and  $x = (0.12–0.15)$  for nominal  $x = 0.12$  [28].

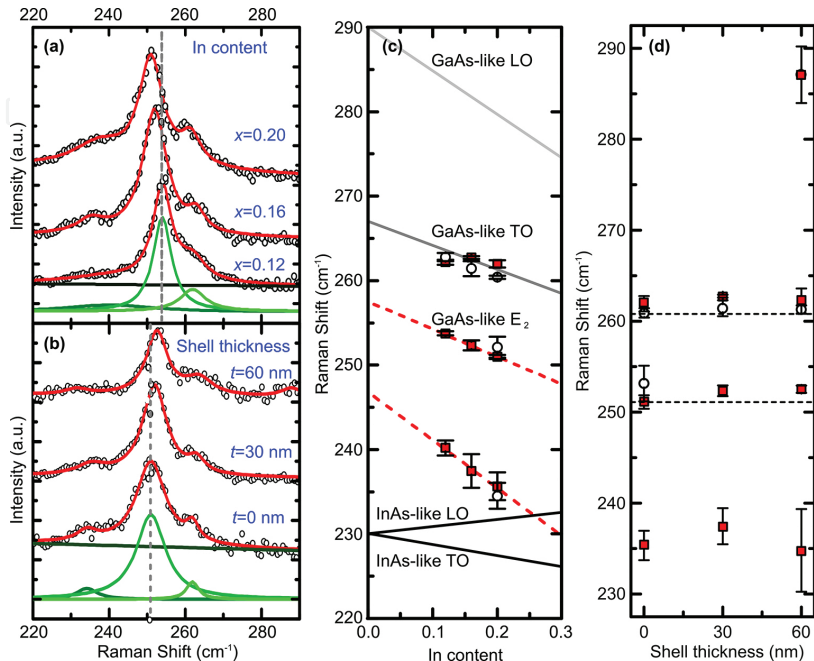


**Figure 9.** (a) Raman spectra (open circles) of  $\text{In}_x\text{Ga}_{1-x}\text{As}$  nanoneedles (with the indicated nominal In content,  $x$ ) capped with 30 nm of GaAs. Spectra were taken in the  $x(yy)\bar{x}$  scattering geometry and were normalized to the GaAs-like  $E_2^H$  phonon peak, whose energy is indicated by a dashed line in the spectra of the  $x = 0.12$  sample. Red solid lines are Lorentzian fits to the data. The single contributions to a Lorentzian fit are represented by green solid lines in the  $x = 0.12$  sample as an example. (b) Same as (a) for samples with the indicated GaAs shell thickness  $t$  and fixed In content ( $x = 0.16$ ). The energy of the GaAs-like  $E_2^H$  phonon is indicated by a dashed line in the spectrum of the sample without shell. (c) Frequency of various optical phonons as a function of indium composition. Symbols represent experimental data points taken under the  $x(zz)\bar{x}$  (open circles) and  $x(yy)\bar{x}$  (full squares) scattering configurations. Solid lines indicate theoretical estimations for ZB  $\text{In}_x\text{Ga}_{1-x}\text{As}$  and dashed lines are linear fits to the data for the GaAs-like and InAs-like  $E_2^H$  modes. (d) Energy of phonon modes for an  $\text{In}_x\text{Ga}_{1-x}\text{As}$  NN with  $x = 0.16$  a function of shell thickness. Symbols represent experimental data points taken under the  $x(zz)\bar{x}$  (full squares) and  $x(yy)\bar{x}$  (open circles) scattering configurations. Dashed lines indicate the energy of the GaAs-like  $A_1/E_1$  (TO) and  $E_2^H$  modes for  $\text{In}_x\text{Ga}_{1-x}\text{As}$  without shell. Reproduced with permission from Ref. [28]. © 2014, American Chemical Society.

In these NNs, the possible presence of strain was also probed by Raman spectroscopy. In **Figure 9(b)**, we display spectra recorded in  $x(yy)\bar{x}$  configuration from NNs with different GaAs shell thickness  $t$  and same indium composition (nominal  $x = 0.16$ ). The peaks' attribution is the same as in panel (a). Here, the GaAs LO phonon mode is also observed, but only in the sample with the thickest shell. Its energy ( $\sim 287 \text{ cm}^{-1}$ ) is downshifted by  $\sim 2 \text{ cm}^{-1}$  with respect to the bulk, which could be due to tensile strain in the shell. The Raman shift of all modes as determined by Lorentzian fits to the spectra (the green solid lines in panel (b) are an example) are reported in panel (d) as full squares for  $x(yy)\bar{x}$  data and open circles for  $x(zz)\bar{x}$  data as a function of the nominal shell thickness. We do not observe any clear and consistent energy variation of the phonon modes with increasing shell thickness, neither an increase in their

FWHM, which allow us to exclude the presence of strain in the core. Possible compositional or shell thickness variations along the NN length can be also excluded, because Raman measurements performed on different points of a same NN do not display significant changes [28].

In this section, it is also worth mentioning that Raman spectroscopy in semiconductor NWs may be used to monitor the incorporation of dopants. At variance with electrical measurements, Raman measurements are not affected by spurious effects coming from the fabrication of contacts. Information on the type and concentration of dopants can be obtained by measuring, respectively, the energy and the intensity of the local vibrational modes associated with the impurities. As an example, we mention Reference [29], where *p*-type GaAs NWs were grown with different silicon doping concentrations and, depending on the growth conditions, the Si<sub>As</sub> local mode (indicative of Si incorporation into As lattice) and the mode due to the formation of neutral Si<sub>As</sub>-Si<sub>As</sub> pairs were observed with different relative weights.

## 6. Resonant Raman scattering in nanowires

In this section, we highlight the power of Resonant Raman scattering (RRS) to investigate the electronic band structure and the electron-phonon interaction in semiconductor NWs. This investigation is possible because the scattering cross section contains the electron-radiation and the electron-phonon interaction Hamiltonians, as well as electronic states for electron-hole pair. In standard conditions, it is very difficult to have access to this information, due to summation over all the intermediate states, but if resonant conditions are achieved, the excitation energy matches electronic interband transitions and the electronic-related terms in the scattering cross section are sizably enhanced. Resonant conditions between excitation energy and electronic states may be reached by varying either the energy of the excitation (using a tunable laser) or the energy of the electronic states (for instance by applying an external pressure at fixed excitation energy). Indeed, the energy gap of semiconductors typically increases with pressure, thus if the pressure dependence of the energy gap is known, pressure-dependent RRS measurements give information on the electronic band structure of the material. We will discuss both methods focusing on InAs NWs with WZ phase [30], because in III-V NWs with WZ phase the electronic band structure is poorly known and RRS has proved to be a necessary tool to shine light on this highly debated topic [31].

**Figure 10(a)** shows some spectra collected from a single WZ InAs NW with growth axis aligned with *z*, as sketched in **Figure 4**, under two scattering configurations,  $x(zz)\bar{x}$  (solid line) and  $x(yy)\bar{x}$  (dashed line). Five different excitation energies comprised between 1.91 and 2.71 eV were used. All spectra exhibit an asymmetric peak at about 216 cm<sup>-1</sup>, in the region of the TO mode, and an LO mode at ~238 cm<sup>-1</sup>, more intense for higher excitation energies. The TO peak is asymmetric because it results from the convolution of two peaks: the A<sub>1</sub>/E<sub>1</sub> (TO) mode at ~218 cm<sup>-1</sup>, dominant in the  $x(zz)\bar{x}$  configuration (where it is mainly A<sub>1</sub>), and the E<sub>2</sub><sup>H</sup> mode at ~214 cm<sup>-1</sup>, dominant for  $x(yy)\bar{x}$ . This is in agreement with the results shown in **Figure 8(b)** for WZ GaAs. In the following we will refer to the convoluted A<sub>1</sub>/E<sub>1</sub> and E<sub>2</sub><sup>H</sup> modes simply as

TO. The measured Raman scattering cross sections (carefully normalized for the spectral response of the setup) of the TO (black squares) and LO (red circles) modes for the configuration  $x(zz)\bar{x}$  (open symbols) and  $x(yy)\bar{x}$  (filled symbols) are shown in panel (b). The intensity of the TO in  $x(zz)\bar{x}$  configuration, that is mainly the  $A_1$  (TO), and of the LO in both configurations, increases with energy in a monotonic way, while the intensity of the TO in  $x(yy)\bar{x}$  configuration (where it is mainly given by the  $E_2^H$  mode), displays a resonance in the 2.41–2.60 eV energy region, which can be correlated with the WZ band structure since the  $E_2^H$  mode is peculiar to WZ phase. Actually, two separate resonances appear, but the number of experimental points is too limited to point out the exact energy at which the maxima occur.

These RRS data can be interpreted at the light of the following considerations. The three lowest energy electronic interband transitions in III–V WZ materials, labeled as A, B, and C, involve

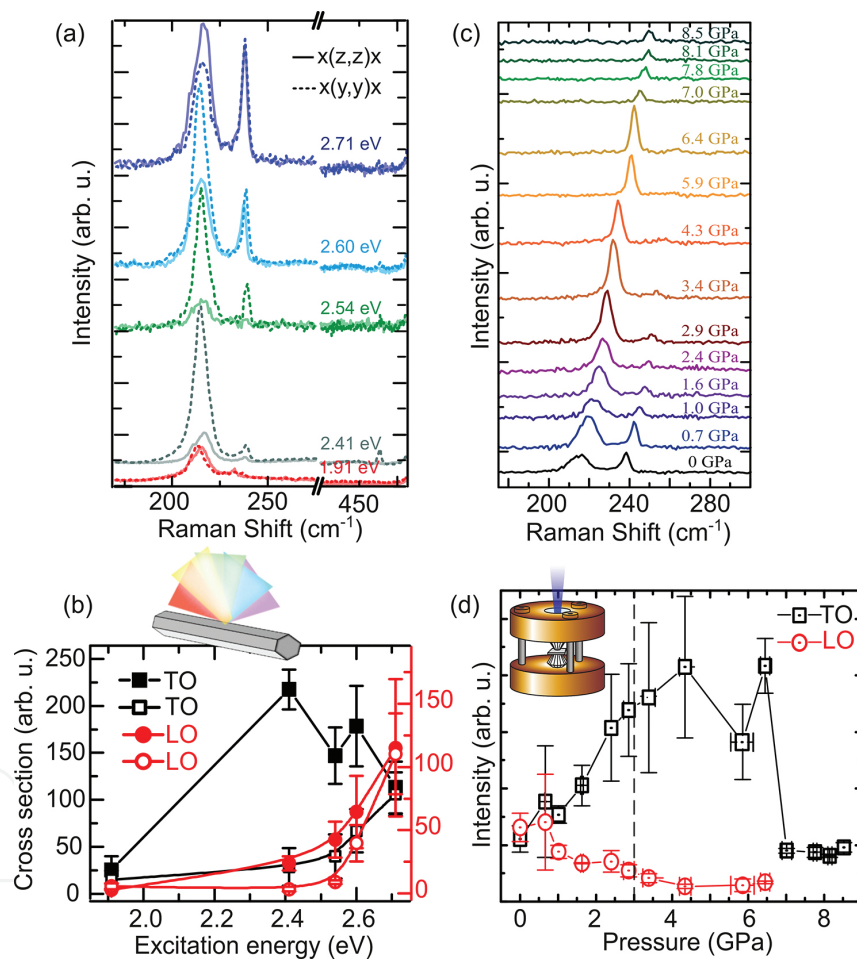


**Figure 10.** Resonant Raman experiments on WZ InAs NWs. (a) Spectra collected on a single NW with five different excitation energies in the  $x(zz)\bar{x}$  (solid line) and  $x(yy)\bar{x}$  (dashed line) configurations. (b) Raman scattering cross section of the TO as defined in the text (black squares and left scale) and LO (red circles and right scale) modes for the configuration  $x(zz)\bar{x}$  (open symbols) and  $x(yy)\bar{x}$  (filled symbols). The error bars come from the average of the Raman scattering cross sections of NWs with four different diameters. Solid lines are guides to the eyes. Reproduced with permission from [30]. Copyright 2013, American Chemical Society. (c) Spectra of a NW bundle for different applied pressures from 0 to 8.5 GPa. Excitation energy is fixed at 2.71 eV. (d) Average on the peaks intensities over two different bundles. The pressure at which the resonance is expected to occur in bulk InAs (based on the known pressure dependence of the  $E_1$  band gap for this excitation energy) is indicated by a dashed line. The solid lines are a guide to the eyes.

the bottommost conduction band minimum, having a  $\Gamma_7^C$  symmetry, and the three valence band maxima, with  $\Gamma_9^V$ ,  $\Gamma_7^V$ , + and  $\Gamma_7^V$ , - symmetries (in order of increasing hole energy). Due to the anisotropy of the hexagonal crystal lattice, there are special selection rules for these transitions: A is allowed only for light polarized perpendicular to the NW growth (like in  $x(yy)\bar{x}$  and  $x(yz, zy)\bar{x}$  configuration), B and C are allowed for both perpendicular and parallel polarized light (like in  $x(yy)\bar{x}$ ,  $x(yz, zy)\bar{x}$ , and  $x(zz)\bar{x}$  configurations). If we consider now the coupling of electronic states with the different phonon mode symmetries, the  $E_2^H$  mode, allowed in  $x(yy)\bar{x}$ , couples with the A transition, while the  $A_1$  mode, in  $x(zz)\bar{x}$ , couples with B and C, and  $E_1$ , in  $x(zy)\bar{x}$ , couples with A, B, and C [30]. According to theoretical calculations on WZ InAs, the  $E_1$  gap at A point involving the first valence band (the one with  $\Gamma_9^V$  symmetry at  $\Gamma$ ) has an energy of  $\sim 2.4$  eV, the  $E_1(A)$  gap involving  $\Gamma_7^V$ , + band has an energy slightly higher than 2.6 eV, and the  $E_1(A)$  gap involving  $\Gamma_7^V$ , - band has a much higher energy. Therefore, the resonance of the TO in  $x(yy)\bar{x}$  (mainly  $E_2^H$ ) at about 2.4 eV can be explained by the coupling between  $E_2^H$  and the  $E_1(A)$  gap involving the first valence band. We stress that the 2.4 eV value of the  $E_1(A)$  gap is reduced with respect to the ZB InAs  $E_1$  gap, in agreement with band structure calculations. The increased intensity with no resonance of the TO in  $x(zz)\bar{x}$  (mainly  $A_1$ ) in the investigated energy region suggests that the resonance could be shifted to energies higher than 2.71 eV, which can be due to the sum of the contributions from the second and the third valence bands.

Let us now discuss high-pressure Raman measurements on the same NWs [30, 32]. Measurements were performed by exciting bundles of NWs with 2.71 eV. Hydrostatic pressure was applied by using a screw clamped opposing-plate diamond Anvil cell (DAC, as the one sketched in **Figure 10(d)**). The NWs were loaded together with a ruby microsphere in a sample chamber located in the center of a stainless steel gasket. A methanol-ethanol mixture (4:1) was used as pressure transmitting medium, and the ruby microsphere was used for determining the pressure through the ruby-fluorescence technique [33]. Raman spectra were collected in backscattering geometry without filtering light polarization, since it is not conserved through the diamond and anyhow the orientation of NWs in the bundle is unknown. Raman spectra collected from an InAs bundle are shown in **Figure 10(c)** for increasing applied pressure up to 8.5 GPa. At ambient pressure (0 GPa), the Raman spectrum is similar to the spectra in panel (a): the broad peak at  $\sim 216$  cm $^{-1}$  is due to convolution of the  $A_1/E_1$  (TO) mode and the  $E_2^H$  TO mode (we continue to label the peak as TO), and the peak at  $\sim 238$  cm $^{-1}$  is due to LO mode. We notice that the frequency of the TO and LO increases with pressure, the FWHM of the TO decreases with pressure, the intensity of the LO peak decreases after 3 GPa and vanishes for pressures higher than 6.4 GPa, and the intensity of the TO increases (with a first maximum around 4 GPa and a second one around 6.5 GPa) and then decreases drastically without vanishing. The absolute intensities of the TO and LO modes (after averaging between two different bundles) are plotted in panel (d) as a function of the applied pressure. Red circles refer to LO, black squares to TO. In bulk ZB InAs, the pressure at which the resonance is expected to occur (based on the known pressure dependence of the  $E_1$  band gap for 2.71 eV

excitation energy) is  $\sim 3$  GPa, as indicated by a dashed line in panel (d). Here, the intensity increase for the TO mode is observed at a pressure slightly higher than 3 GPa due to a value of the  $E_1$ -gap slightly lower than the 2.71 eV. This finding confirms the results obtained by the energy-dependent Raman study. Indeed, assuming for the  $E_1$  WZ band gap the same pressure dependence of the  $E_1$  ZB gap and an energy gap at ambient pressure of 2.4 eV as the one determined from data in **Figure 10(b)**, the resonance is expected at about 4.2 GPa, in good agreement with the measurements. Moreover, the continuous decrease in intensity of the LO mode with pressure agrees with what expected from a gap which is already bigger than 2.71 eV at ambient pressure: with increasing pressure, and consequently increasing the relevant energy gap, the LO mode is going far and far from resonance conditions, leading to a continuously decreased intensity. This confirms its coupling with the gaps from the second and third valence bands at the A point. The disappearance of the LO mode at 6.4 GPa could be related to the structural phase transition that occurs in the ZB material, associated with the metallization of the system. We point out that the spectrum could be fully recovered after depressurizing the DAC, indicating a reversible structural transition.

We have shown that the present method, based on the combination of two RRS techniques, has proved to be a novel and powerful experimental tool for band structure investigation of nanoscale semiconductors.

In conclusion, we have provided valuable examples, mostly based on our experimental results, of how powerful is Raman spectroscopy in investigating all the most important aspects of the lattice dynamics of semiconductor nanowires.

## Acknowledgements

The authors acknowledge S. Yazji and G. Abstreiter of Walter Shottky Institute of the Technische Universität München, A. Fontcuberta i Morral of the École Polytechnique Fédérale de Lausanne, and P. Postorino of Sapienza University of Rome for their precious contribution to data acquisition and interpretation. We acknowledge financial support from the Swiss National Science Foundation research grant (Project Grant No. 200021\_165784).

## Author details

Marta De Luca and Ilaria Zardo\*

\*Address all correspondence to: ilaria.zardo@unibas.ch

Department of Physics, University of Basel, Basel, Switzerland

## References

- [1] Yazawa M, Koguchi M, and Hiruma K. Heteroepitaxial ultrafine wire-like growth of InAs on GaAs substrates. *Applied Physics Letters*. 1991;58:1080.
- [2] Hayden O, Agarwal R, and Lu W. Semiconductor nanowire devices. *Nanotoday*. 2008;3:12.
- [3] Plissard S R, Slapak D R, Verheijen M A, Hocevar M, Immink G W G, van W I, Nadj-Perge S, Frolov S M, Kouwenhoven L P, and Bakkers E P A M. From InSb nanowires to nanocubes: Looking for the sweet spot. *Nano Letters*. 2012;12(4):1794–1798.
- [4] De Luca M. Optical Studies in Semiconductor Nanowires. 1st ed. Roma: Sapienza Università Editrice; 2015. 248 p.
- [5] Subramaniam M R, Devanathan S, and Kumaresan D. Synthesis of micrometer-sized hierarchical rutile TiO<sub>2</sub> flowers and their application in dye sensitized solar cells. *RSC Advances*. 2014;4:36791.
- [6] Wagner R S and Ellis W C. Vapor-liquid-solid mechanism of single crystal growth. *Applied Physics Letters*. 1964;4:89.
- [7] Dasgupta N P, Sun J, Liu C, Brittman S, Andrews S C, Lim J, Gao H, Yan R, and Yang P. 25th anniversary article: Semiconductor nanowires—synthesis, characterization, and applications. *Advanced Materials*. 2014;26:2137–2184.
- [8] Dey A W, Svensson J, Borg B M, Ek M, and Wernersson L-E. Single InAs/GaSb nanowire low-power CMOS inverter. *Nano Letters*. 2012;12:5593.
- [9] Rossi N, Braakman F R, Cadeddu D, Vasyukov D, Tütüncüoglu G, Fontcuberta i Morral A, Poggio M. Vectorial scanning force microscopy using a nanowire sensor. *Nature Nanotechnology* (in press). DOI: 10.1038/NNANO.2016.189.
- [10] Weisse J M, Lee C H, Kim D R, and Zheng X. Fabrication of flexible and vertical silicon nanowire electronics. *Nano Letters*. 2012;12:3339.
- [11] Ra Y-H, Wang R, Woo S Y, Djavid M, Sadaf S M, Lee J, Botton G A, and Mi Z. Full-color single nanowire pixels for projection displays. *Nano Letters*. 2016;16:4608.
- [12] Yazji S, Swinkels M Y, De L M, Hoffmann E A, Ercolani D, Roddaro S, Abstreiter G, Sorba L, Bakkers E P A M, and Zardo I. Assessing the thermoelectric properties of single InSb nanowires: The role of thermal contact resistance. *Semiconductor Science and Technology*. 2016;31:064001.
- [13] Krogstrup P, Jørgensen H I, Heiss M, Demichel O, Holm J V, Aagesen M, Nygard J, and Fontcuberta i Morral A. Single-nanowire solar cells beyond the Shockley–Queisser limit. *Nature Photonics*. 2013;7:306.
- [14] Sahoo P K, Janissen R, Monteiro M P, Cavalli A, Murillo D M, Merfa M V, Cesar C L, Carvalho H F, de Souza A A, Bakkers E P A M, and Cotta M A. Nanowire arrays as cell

- force sensors to investigate adhesin-enhanced holdfast of single cell bacteria and biofilm stability. *Nano Letters*. 2016;16:4656–4664. DOI: 10.1021/acs.nanolett.6b01998
- [15] Turrel G and Corset J, editors. *Raman Microscopy Developments and Applications*. 1st ed. Malta: Academic Press; 1996. 463 p.
  - [16] Xiang Y, Zardo I, Cao L Y, Garma T, Heiss M, Morante J R, Arbiol J, Brongersma M, and Fontcuberta i Morral A. Spatially resolved Raman spectroscopy on indium-catalyzed core-shell germanium nanowires: Size effects. *Nanotechnology*. 2010;21:105703.
  - [17] Spirkoska D, Abstreiter G, and Fontcuberta i Morral A. Size and environment dependence of surface phonon modes of gallium arsenide nanowires as measured by Raman spectroscopy. *Nanotechnology*. 2008;19:435704.
  - [18] Zardo I, Abstreiter G, and Fontcuberta i Morral A. Raman spectroscopy on semiconductor nanowires. In: Paola Prete, editor. *Nanowires*. InTech; 2010. DOI: 10.5772/39514. Available from <http://www.intechopen.com/books/nanowires/raman-spectroscopy-on-semiconductor-nanowires>
  - [19] Zardo I, Conesa-Boj S, Peiro F, Morante J R, Arbiol J, Uccelli E, Abstreiter G, and Fontcuberta i Morral A. Raman spectroscopy of wurtzite and zinc-blende GaAs nanowires: Polarization dependence, selection rules, and strain effects. *Physical Review B*. 2009;80:245324.
  - [20] Ruda H E and Shik A. Polarization-sensitive optical phenomena in semiconducting and metallic nanowires. *Physical Review B*. 2005;72:115308.
  - [21] De Luca M, Zilli A, Fonseka H A, Mokkapati S, Miriametro A, Tan H H, Smith L M, Jagadish C, Capizzi M, and Polimeni A. Polarized light absorption in wurtzite InP nanowire ensembles. *Nano Letters*. 2015;15:998–1005.
  - [22] Glas F, Harmand J-C, and Patriarche G. Why does wurtzite form in nanowires of III-V zinc blende semiconductors? *Physical Review Letters*. 2007;99:146101.
  - [23] Caroff P, Bolinsson J, and Johansson J. Crystal phases in III–V nanowires: From random toward engineered Polytypism. *IEEE Journal of Selected Topics. Quantum Electronics*. 2011;17:829.
  - [24] Akopian N, Patriarche G, Liu L, Harmand J-C, and Zwiller V. Crystal phase quantum dots. *Nano Letters*. 2010;10(4):1198–1201.
  - [25] Assali S, Gagliano L, Oliveira D S, Verheijen M A, Plissard S R, Feiner L F, and Bakkers E P A M. Exploring crystal phase switching in GaP nanowires. *Nano Letters*. 2015;15:8062.
  - [26] Murayama M and Nakayama T. Chemical trend of band offsets at wurtzite/zinc-blende heterocrystalline semiconductor interfaces. *Physical Review B*. 1994;49:4710.
  - [27] Loudon R. The Raman effect in crystals. *Advanced Physics*. 1964;13:423–482.

- [28] Wang X, Zardo I, Spirkoska D, Yazji S, Ng K W, Ko W, Chang-Hasnain C, Finley J, and Abstreiter G. Valence band splitting in wurtzite InGaAs nanoneedles studied by photoluminescence excitation spectroscopy. *ACS Nano*. 2014;8:11440.
- [29] Ketterer B, Mikheev E, Uccelli E, and Fontcuberta i Morral A. Compensation mechanism in silicon-doped gallium arsenide nanowires. *Applied Physics Letters*. 2010;97:223103.
- [30] Zardo I, Yazji S, Hörmann N, Hertenberger S, Funk S, Mangialardo S, Koblmüller G, Postorino P, and Abstreiter G. E1(A) Electronic band gap in wurtzite InAs nanowires studied by resonant Raman scattering. *Nano Letters*. 2013;13:3011.
- [31] Ketterer B, Heiss M, Uccelli E, Arbiol J, and Fontcuberta i Morral A. Untangling the electronic band structure of wurtzite GaAs nanowires by resonant Raman spectroscopy. *ACS Nano*. 2011;5:7585.
- [32] Yazji S, Zardo I, Hertenberger S, Morkötter S, Koblmüller G, Abstreiter G, and Postorino P. Pressure dependence of Raman spectrum in InAs nanowires. *Journal of Physics: Condensed Matter*. 2014;26:235301.
- [33] Mao H K, Xu J, and Bell P M. Calibration of the ruby pressure gauge to 800 kbar under quasi-hydrostatic condition. *Journal of Geophysical Research*. 1986;91:4673–4676.

